Available online at https://link.springer.com/journal/42241
http://www.jhydrodynamics.com
Journal of Hydrodynamics, 2022, 34(4): 647-664
https://doi.org/10.1007/s42241-022-0054-z

Numerical study of fluid resonance of a two-dimensional heaving-free moonpool in a wide range of incident waves

Peng-lin Jing[1], Guang-hua He[1, 2, 3], Zheng-xiao Luan[1], Chao-gang Liu[1], Hao Yang[1]
1. *School of Mechatronics Engineering, Harbin Institute of Technology, Harbin 150001, China*
2. *School of Ocean Engineering, Harbin Institute of Technology, Weihai, Weihai 264209, China*
3. *Shandong Institute of Shipbuilding Technology, Weihai 264209, China*

(Received March 30, 2022, Revised May 25, 2022, Accepted June 4, 2022, Published online August 25, 2022)

Abstract: The fluid resonance of a moonpool freely heaving in a beam sea is studied by an in-house constrained interpolation profile (CIP) code. Generally, the moonpool behaves as in the piston mode with a narrow opening. The numerical studies are carried out for a wide range of the incident waves, and a new secondary resonant region is identified in the low frequency region of the incident waves, besides the ordinary main resonant region. Numerical results demonstrate that the horizontal wave forces are significant in the secondary resonant region, although the resonant wave elevations are less remarkable than those of the main resonant region. It is concluded that the fluid resonance of the low frequency is excited mainly by the heave motion of the moonpool. Parameter studies of the moonpool draft and the gap width of the moonpool based on the fluid resonance are also performed.

Key words: Gap resonance, low-frequency incident wave, heave motion, constrained interpolation profile (CIP)

Introduction

Narrow gaps commonly exist in marine structures. When the structures are operated at certain wave frequencies, the wave elevation in the narrow gap may be greatly enlarged, therefore, leading to a remarkable increase of the wave loads. Such phenomenon is known as the 'gap resonance', which becomes an interesting topic due to its importance in engineering applications and attracts a great deal of attention in the field of marine hydrodynamics.

The potential-flow-based methods were widely used in solving gap-resonance problems of floating structures. The boundary element method[1], the higher-order boundary element method[2] and the scaled boundary finite-element method[3] were implemented to investigate the gap-resonance problem. The resonant frequency for fixed bodies was predicted by ignoring the motion response of floating structures. With these methods, the resonant free-surface elevation in the gap and the wave forces on the floating bodies are always overestimated, due to the ignoring of the fluid viscosity and the vortex shedding[4-5]. To overcome this problem, several numerical techniques were implemented by using an artificial energy dissipation term in the potential-flow models[6-8], which could improve the accuracy by tuning the artificial dissipation coefficient. However, it is not easy to find a unique value of the artificial dissipation coefficient without experimental data. So far, those artificial dissipation coefficients were usually determined based on the experimental measurements[9-10].

Due to the rapid development of the computational techniques in recent years, the computational fluid dynamic (CFD) method has become a powerful approach to predict both the resonant frequency and the wave elevation well[11-12]. The CFD methods in principle provide an adequate description of the physics of the concerned problem, however, the balance between the accuracy and the efficiency of the CFD simulations is a challenging topic. While the numerical accuracy and efficiency are quite different for different CFD solvers, an accurate and efficient CFD solver is desirable for engineers and scholars. Compared to the conventional upwind scheme, the constrained interpolation profile (CIP) scheme provides much more accurate numerical results, with a third-order polynomial to approximate the unknowns on the grid point. This method was firstly proposed by Takewaki et al.[13], and then Hu and Kashiwagi[14] firstly introduced the CIP method into the field of marine hydrodynamics to simulate extremely non-

Biography: Peng-lin Jing (1995-), Male, Ph. D. Candidate,
E-mail: hitwhjpl@163.com
Corresponding author: Guang-hua He,
E-mail: ghhe@hitwh.edu.cn

linear free-surface flows. Zhao et al.[15], He[16] applied the CIP method to investigate the strong nonlinear pro- blems such as the dam break and the seakeeping. With the developed CIP method, the resonant frequency and the free-surface elevation at the gap of two or three fixed side-by-side hulls can well be predicted[17].

For the gap-resonance problem, most studies focused on the side-by-side multiple floating structures to serve as the motion-fixed condition. However, the floating structures always have motions induced by waves. The radiation and diffraction problems of a two-dimensional moonpool-type structure were widely studied by the analytical methods[18], the experimental measurements[18], the viscosity numerical models[12] and other methods. The forced oscillation studies can provide the fundamental information of the hydrodynamic properties of the floating structure, which could be used as the basis to study the problems of wave-structure interactions[19-20]. However, the forced oscillations are still quite different from the motion free situation. Some efforts were made by considering the wave-induced motion response, for example, the floating ship moored beside wharfs[21], the sway-free barge near a fixed barge[22], the heaving-free moonpool with a wide gap[6] and a narrow gap[5] in the beam sea, and the recessing type moonpool of a floating drilling vessel[23]. The moonpool gap-resonances under the fixed and motion-free assumptions do show quite different characteristics.

Although the above studies did provide important insights into the gap-resonance problem, most of them focused on the resonance of the moderate incident waves or the moonpools with a large horizontal opening. In view of the fact that the long wave excitation also exists commonly in a real application, the present study deals with the problem of a two-dimensional rectangular moonpool with a narrow gap freely heaving under a wide range of the beam sea. The fluid resonance in the moonpool is generally shown in two forms, the piston mode and the sloshing mode[24], while it is always in the piston mode in a narrow gap, which is the case in the present study. A CIP-based viscous nonlinear numerical wave tank is developed for simulating the gap-resonance problem. Particular attention is paid to the fundamental mechanism of the secondary resonant region by investigating the free-surface elevation at the gap and the wave loads on the heaving-free moonpool combined with parameter studies.

1. Numerical models

The fluid is assumed incompressible and homogeneous viscous, the governing equations are given by the continuity equation and the Navier-Stokes equations, as follows:

$$\frac{\partial u_i}{\partial x_i} = 0 \tag{1}$$

$$\frac{\partial u_i}{\partial t} + u_j \frac{\partial u_i}{\partial x_j} = -\frac{1}{\rho}\frac{\partial p}{\partial x_i} + \nu \frac{\partial^2 u_i}{\partial x_j \partial x_j} + f_i \tag{2}$$

where i, j represent the cell address in x- or y-directions, u_i is the velocity component in x_i-coordinate direction, ρ is the density of the fluid, p is the pressure, ν is the kinematic viscosity and f_i denotes the body forces such as the gravity force.

1.1 *CIP numerical scheme*

The CIP scheme is an enhanced numerical approach to provide a much more accurate numerical result compared to the conventional upwind scheme by using a third-order polynomial to approximate the unknowns on the grid points. This means that to achieve a certain computational accuracy, a smaller number of grids may be used by the CIP scheme than by the conventional high-order upwind schemes. Figure 1 shows a schematic comparison between the conventional upwind scheme and the present CIP method (in one-dimensional case). As can be seen, in the upwind scheme, the function profile is constructed by a linear interpolation (Fig. 1(a)), whereas in the CIP scheme, it is constructed by the third-order polynomial fitting (Fig. 1(b)). For the advection computation of a variable f, both the transportation equation of f and the transportation equation of its spatial gradient, $g_i = \partial f / \partial x$, are used at the same time. Here, f represents each of ρ, μ_i and p in Eqs. (1), (2), respectively. The transportation equation of f is given as

$$\frac{\partial f}{\partial t} + u_i \frac{\partial f}{\partial x} = H \tag{3}$$

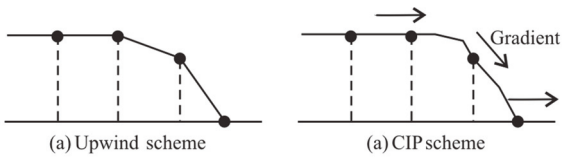

Fig. 1 Principle of the CIP method

The transport equation of g_i can be obtained by differentiating equation (3)

$$\frac{\partial g_i}{\partial t} + u_j \frac{\partial g_i}{\partial x_j} = \frac{\partial H}{\partial x_i} - g_j \frac{\partial u_j}{\partial x_i} \tag{4}$$

More details about this CIP method can be found in Refs. [14, 25, 16].

1.2 *Internal wave maker*

The internal wave maker using a momentum source function[26] is employed to generate the targeted waves in the present numerical model. The x-coordinate momentum source term S_x^{mom} can be written as

$$S_x^{\text{mom}} = -g(2\beta x)\exp(-\beta x^2)\frac{D}{\omega}\sin(-\omega t) \tag{5}$$

where x is the x-axis, t is the time, ω is the angular frequency and β is the source width parameter. The source amplitude D can be determined by

$$D = \frac{2A_0(\omega^2 - \alpha_1 g k^4 h^3)\cos\theta}{\omega I_1[1-\alpha(kh)^2]} \tag{6}$$

where h is the water depth, k is the wave number, θ is the wave direction, A_0 is the wave amplitude are the wave parameters used to generate a target wave train and $I_1 = \sqrt{\pi/\beta}\exp(-k^2/4\beta)$. α_1, α are the parameters in the Boussinesq equations

$$\alpha_1 = \alpha + \frac{1}{3} \tag{7}$$

$$\alpha = \frac{z_\alpha}{h}\left(\frac{z_\alpha}{2h}+1\right) \tag{8}$$

where z_α is a representative velocity vector at a position in a depth-averaged model and is usually expressed as $z_\alpha = -0.530h$.

The present numerical model involves the liquid, the gap and the solid phases and they represent the water, the air and the floating body, respectively. A tangent of hyperbola for interface capturing (THINC) method is adopted to capture the gas-liquid interface, whereas a virtual particle method is used for capturing the floating-body surface. More details of the THINC scheme and the virtual particle method could be found in Refs. [27, 25], respectively.

2. Convergence study of the developed CIP model

2.1 *Arrangement and mesh generation*

The computational model for a heaving-free moonpool is shown in Fig. 2, which is made up of two identical boxes for the simulations. The two parts of the moonpool are named Body-A, Body-B for convenience. In Fig. 2, h denotes the water depth, B, d and B_g denote the width of each body, the draft of the body, and the width of the narrow gap, respectively. It should be noticed that in all simulations the body width and the water depth are kept constant as $B = 0.5$ m, $h = 0.5$ m. Also, the incident wave height is kept as $H_0 = 0.024$ m.

Non-uniform meshes are adopted in the current simulations to divide the computational domain into several subregions to save the computational resource. Figure 3 presents the grid arrangement around the moonpool. Six refinement zones are employed for accurate and efficient simulations. Zone 2 is for the free-surface capturing and the incident waves, the other Zones around the moonpool directly influence the motion response and the hydrodynamic resonance. Corresponding verification is detailed in the sub-section 2.2. The damping region is always twice longer than the incident wave length, where the grid size gradually increases to help dissipate the wave reflection. Corresponding wave-damping techniques can be found in Ref. [14].

2.2 *Convergence study*

The convergence studies with respect to the time step and the grid size are carried out using the correlation factor method. Once a parameter is considered in the convergence study, all other input parameters are kept constant. Three solutions with the refined time step and grid size are obtained. Constant refinement ratios of $\sqrt{2}$, 2 for the grid size and the time step are applied, respectively. It should be noticed that the mentioned grid size is of the cells around the floating bodies (zone 1, zones 3-6 in Fig. 3), since the grid arrangement around the free surface has already been verified by generating high-quality regular waves[28-29]. All tested cases are shown in Table 1.

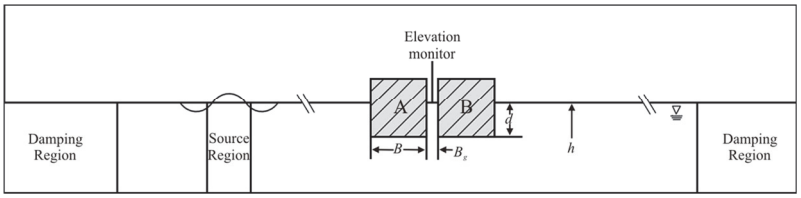

Fig. 2 Computational domain arrangement

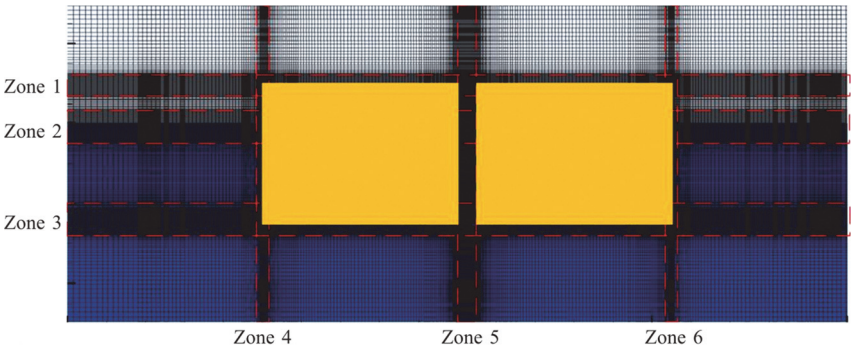

Fig. 3 (Color online) Computational grid around moonpool

Table 1 Setup of grid size and time step for the uncertainty verification (constant refinement ratio of $\sqrt{2}$ for grid size and 2 for time step

Convergence setup	Grid Size $(x \times y)$	Time step
Fine (S_1)	0.707 mm×0.354 mm	T_0 / 4000
Medium (S_2)	1.000 mm×0.500 mm	T_0 / 2000
Coarse (S_3)	1.414 mm×0.707 mm	T_0 /1000

The present study follows the procedure suggested by Wang et al.[30] to estimate the numerical uncertainty of the developed numerical model. It is assumed that the iterative errors are negligible compared to the convergence errors. The present study of a heaving-free moonpool excited by regular incident waves focuses on the gap-resonance phenomenon, the free-surface elevation at the gap (briefly, the gap elevation) and the response amplitude operator of the heaving-free moonpool (briefly, the heave RAO) are selected as the variables for the procedure. The variations of the gap elevations and the heave RAOs between the shown grid arrangements (Table 1) for the input parameter can be calculated as:

$$\sigma_{21}=S_2-S_1 \tag{9}$$

$$\sigma_{32}=S_3-S_2 \tag{10}$$

The convergence ratio is defined as follows

$$R=\frac{\sigma_{21}}{\sigma_{32}} \tag{11}$$

where S_1, S_2 and S_3 are the solutions from the fine, medium and coarse cases, respectively. The convergence ratio is the key to judging the convergence conditions: (1) Monotonic convergence $(0<R<1)$, (2) Oscillatory convergence ($R<0$, $|R|<1$), (3) Monotonic divergence $(R>1)$, (4) Oscillatory divergence ($R<0$, $|R|>1$).

Numerical uncertainties are predicted by calculating the error based on the oscillation with the maximum and minimum solutions under the condition (2), the errors and the uncertainties cannot be estimated under the conditions (3), (4), under the condition (1), the numerical errors and uncertainties can be estimated by the generalised Richardson extrapolation as follows:

$$\varepsilon^*_{RE_1}=\frac{\sigma_{21}}{r^p-1} \tag{12}$$

$$p=\frac{\ln(\sigma_{32}/\sigma_{21})}{\ln(r)} \tag{13}$$

where $\varepsilon^*_{RE_1}$ is a one-term numerical error, p is the order of accuracy, r is the specific refinement ratio for the input parameter. To account for the effects of high-order terms on the error and uncertainty estimates, a correction factor is employed as follows

$$C=\frac{r^p-1}{r^{p_{\text{est}}}-1} \tag{14}$$

where p_{est} is an estimate for the limiting order of accuracy. Therefore, Eq. (12) can be improved by this correction factor as

$$\varepsilon^*=C\varepsilon^*_{RE_1} \tag{15}$$

The uncorrected uncertainty δ and the corrected uncertainty δ_c are determined by the following equations depending on the distance of the solutions to the asymptotic range as follows:

$$\delta=(9.6[1-C)^2+1.1]\left|\varepsilon^*_{RE_1}\right|,\ |1-C|<0.125 \tag{16a}$$

$$\delta=\left(2|1-C|+1\right)\left|\varepsilon^*_{RE_1}\right|,\ |1-C|\geq 0.125 \tag{16b}$$

$$\delta_c = [2.4(1-C)^2 + 0.1]\left|\varepsilon^*_{RE_1}\right|, \quad |1-C| < 0.25 \tag{17a}$$

$$\delta_c = \left(|1-C|\right)\left|\varepsilon^*_{RE_1}\right|, \quad |1-C| \geq 0.25 \tag{17b}$$

A typical incident wave frequency of $kh = 1.80$ with the wave height of $H_0 = 0.024$ m is adopted with the moonpool settings as $d = 0.252$ m, $B_g = 0.05$ m, as presented in Fig. 2. Numerical uncertainty estimations based on the time step and the grid size are shown in Table 2 (the subscript T represents the estimation of the time step) and Table 3 (the subscript G represents the estimation of the grid size), respectively. Corresponding gap elevation and heave motion in both cases are shown in Figs. 4, 5, respectively. The results indicate that with the present numerical model, the monotonic convergence is reached in both cases of the time step and the grid size. The gap elevation is sensitive for both the time-step resolution and the grid size resolution, and the heave motion is more sensitive for the grid resolution. A reasonably low level of the uncertainty is observed for both the time step and the grid size with respect to the two selected solutions. The maximum uncertainty level of 3.414% is obtained for the gap elevation in the grid-size convergence calculation.

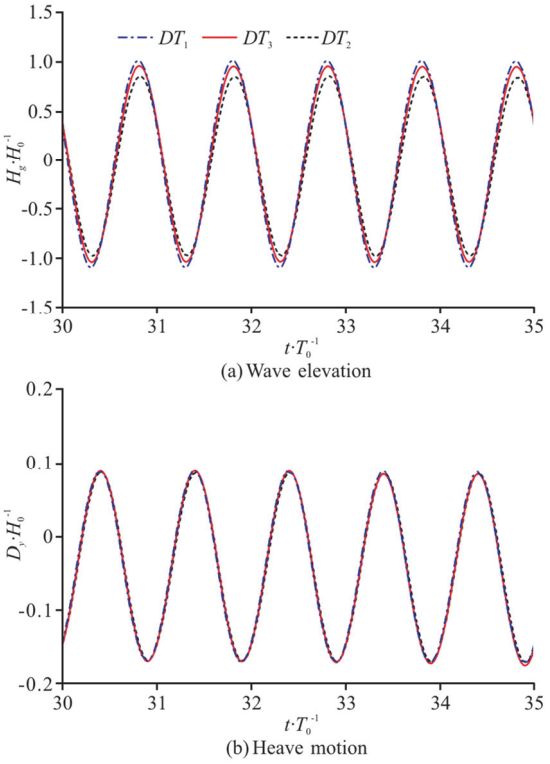

Fig. 4 (Color online) Convergence study based on time step ($kh = 1.80$, $d = 0.252$ m, $B_g = 0.05$ m and $H_0 = 0.024$ m)

2.3 *Validation of the CIP model*

Since the CIP model enjoys a high accuracy in predicting the cases with strong-nonlinear wave-body interactions[25], the present validation focuses on the gap resonance of the fixed moonpool with a quite narrow gap using the verified model presented in the sub-section 2.2. The computational arrangement is the same as the experimental settings[31], with $B = 0.5$ m, $B_g = 0.05$ m, $d = 0.252$ m, $h = 0.5$ m and $H_0 = 0.024$ m as shown in Fig. 2. The comparisons of the resonant frequency and the gap elevation for the fixed moonpool between the present model and the published

Table 2 Numerical uncertainty for time step ($kh = 1.80$, $d = 0.252$ m, $B_g = 0.05$ m and $H_0 = 0.024$ m)

Variable	Solution			Convergence ratio	Uncertainty		
	S_{T1}	S_{T2}	S_{T3}	R_T	ε^*_T ($\%S_{T1}$)	δ_T ($\%S_{T1}$)	δ_{Tc} ($\%S_{T1}$)
H_g / H_0	2.065	2.001	1.823	0.357	1.025	3.075	0.683
D_y / H_0	0.261	0.260	0.257	0.515	0.178	1.348	0.390

Table 3 Numerical uncertainty for grid size ($kh = 1.80$, $d = 0.252$ m, $B_g = 0.05$ m and $H_0 = 0.024$ m)

Variable	Solution			Convergence ratio	Uncertainty		
	S_{G1}	S_{G2}	S_{G3}	R_G	ε^*_G ($\%S_{G1}$)	δ_G ($\%S_{G2}$)	δ_{Gc} ($\%S_{G2}$)
H_g / H_0	2.038	2.001	1.638	0.101	1.809	3.414	1.605
D_y / H_0	0.261	0.260	0.255	0.208	0.409	0.711	0.302

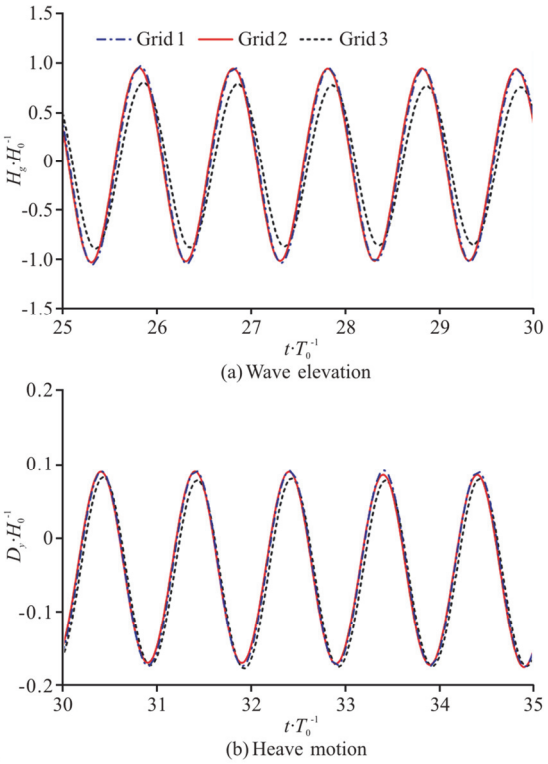

Fig. 5 (Color online) Convergence study based on grid size ($kh = 1.80$, $d = 0.252$ m , $B_g = 0.05$ m and $H_0 = 0.024$ m)

data are shown in Fig. 6, and the corresponding detailed data and the relative errors are shown in Table 4. The relative errors are calculated as follows:

$$\mu = \left| \frac{\alpha_i - \alpha_{\text{exp}}}{\alpha_{\text{exp}}} \right| \times 100\% \tag{18}$$

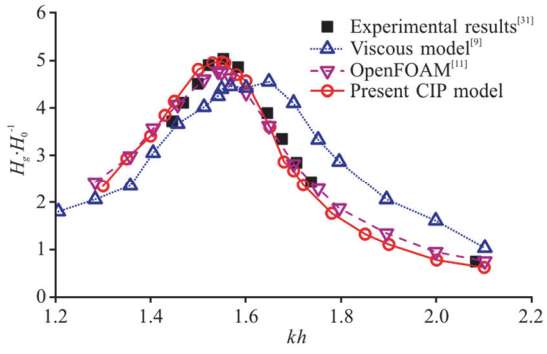

Fig. 6 (Color online) Comparison of gap elevation for the fixed moonpool between the present calculation results and the published data (H_g is the computed wave elevation at the narrow gap, H_0 is the height of the incident waves)

Table 4 Comparison of resonant frequency and amplitude for the fixed moonpool between the present results and the published data

	kh	μ_1 /%	H_g / H_0	μ_2 /%
Experimental results[31]	1.552	-	5.0365	-
Viscous model[9]	1.643	5.811	4.5558	9.544
Open FOAM[11]	1.541	0.721	4.7721	5.250
Present CIP model	1.550	0.169	4.9780	1.162

where μ is the relative error between the experimental and numerical results, α_{exp} is the experimental result and α_i is the i-th numerical result, including both the resonant frequency and the gap elevation.

It is indicated that the developed CIP method gives results in better agreement with the published experimental data[31] than other viscous models[9, 11], for all incident wave frequencies. Especially the relative differences of the resonance frequency and its amplitude are only 0.169%, 1.162%, respectively. It is shown that the present CIP-based model is powerful in solving the hydrodynamic resonance of the moonpool with a narrow gap.

3. Numerical results and discussions

3.1 *Hydrodynamic resonance for heaving-free moonpool of different gap widths*

3.1.1 Gap resonance of the moonpool

With the notations used in Fig. 2, this moonpool consists of two identical rectangular bodies namely Body-A and Body-B, and $d = 0.252$ m , $B = 0.5$ m , $h = 0.5$ m and $H_0 = 0.024$ m . The gap width between these two bodies is chosen to be a variable and its influence is to be investigated with $B_g = 0.03$ m, 0.05 m and 0.07 m, corresponding to the ratio of the gap breath to the body breath of 0.06, 0.1 and 0.14, respectively. It should be pointed out that in the present study, only the heave motion of the moonpool is considered.

Figure 7 shows the non-dimensional wave elevation in the narrow gap (briefly, the gap elevation) with different gap widths. The gap elevation obtained by the STAR-CCM+ with $B_g = 0.05$ m is also shown in Fig. 7 for validating the results in the lower frequency region. These two models give results in good agreement in predicting the resonant frequencies and amplitudes, here, we focus on the lower frequency region. More details of the numerical model based on

the STAR-CCM+ can be found in Ref. [5]. The gap elevation and the relative error between the two numerical models are listed in Table 5. Reasonable agreement is reached between them, the relative errors are always less than 4%, which provides further validation for the present CIP results, since the STAR-CCM+ is based on the finite volume method, whereas the CIP model is based on the finite difference method.

To highlight the phenomenon in the lower frequency region of the incident waves, the results for the fixed moonpool with the arrangement of B_g = 0.05 m are shown for a comparison. Figure 7 indicates that the fixed moonpool has only one resonant region of the fluid resonance, whereas for the heaving-free moonpool, two such regions can be identified. It is noted that the two kinds of moonpools are both in the piston mode. The resonant region with a higher wave frequency shows a larger resonant magnitude for the fluid resonance, which is called the "main resonant region" for convenience. While the other one, which locates in a lower frequency region with a weaker amplitude, is called the "secondary resonant region" for convenience. Detailed resonant frequencies and amplitudes under all presented conditions are given in Table 6. For the heaving-free moonpool, the fluid resonance in the main resonant region is more sensitive to the change of the gap width, while the gap width affects little the fluid resonance in the secondary resonant region, these three curves are almost identical when kh is less than 1.3. For the heaving-free moonpool, the resonant frequency in the main resonant region increases with the decrease of B_g, which shows a similar pattern as that in the fixed moonpool.

However, there is no secondary resonant region in the fixed moonpool, the gap elevation continues to decrease and nearly approaches 1 with the decrease of kh. The wave energy is almost consumed by the wave reflection and the wave transmission, with almost none left to excite the gap water[11]. The only difference between the simulations of the fixed moonpool and the heaving-free moonpool is that the heave motion is allowed in one and not allowed in the other. Detailed discussions of the contribution of the heave response are presented in Section 3.2.

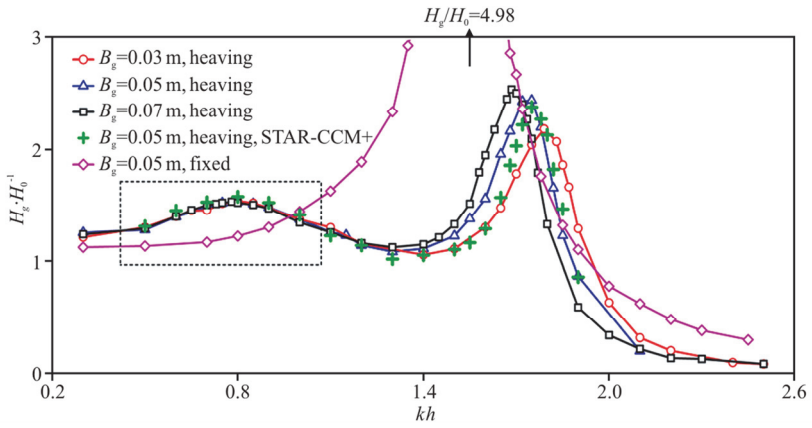

Fig. 7 (Color online) Wave elevation in the narrow gap of different gap widths

Table 5 Comparison of the wave elevation at the gap (H_g / H_0) between the present CIP model and STAR-CCM+ in the lower frequency region (d = 0.252 m, B_g = 0.05 m)

kh	0.50	0.60	0.70	0.80	0.90	1.00	1.10	1.20
Present CIP model	1.31	1.46	1.53	1.58	1.53	1.42	1.23	1.14
STAR-CCM+	1.28	1.40	1.51	1.57	1.48	1.38	1.26	1.14
Relative error/%	2.48	3.99	1.38	2.78	2.79	2.88	2.38	0.02

Table 6 Resonant frequencies and amplitudes for different gap widths (d = 0.252 m)

		B_g = 0.03 m	B_g = 0.05 m	B_g = 0.07 m	B_g = 0.05 m (fixed)
The secondary resonant region	kh	0.80	0.80	0.78	-
	H_g / H_0	1.54	1.54	1.54	-
The main resonant region	kh	1.79	1.75	1.69	1.55
	H_g / H_0	2.19	2.45	2.54	4.98

3.1.2 Heave response of the moonpool

The heave RAOs of the moonpool in three different gap widths are shown in Fig. 8. To see the influence of the existence of the gap on the heave response of the moonpool, a series of cases without the gap are shown also in Fig. 8, with the same computational arrangement except for the gap, i.e., one single box with body width 1.050 m and body draft 0.252 m.

There is only one maximum value in the no-gap case (single body), which is located in the secondary resonant region, while the maximum values of the RAO occur in both the main and the secondary resonant regions for the moonpool. Detailed maximum values and their frequencies of the heave RAOs are shown in Table 7. In the secondary resonant region, the heave RAOs of the moonpool are slightly larger than those in the no-gap cases. This may be due to the amplified gap elevation. In the secondary resonant region, the gap width affects little the heave RAO. In view of the fact that the moonpool can freely heave under the wave excitation, the Body-A and the Body-B heave together, hence the characteristic length (L) of the whole body is equal to $L = 2B + B_g$. While the gap width changes from 0.03 m to 0.07 m, the increment ratio of the characteristic length is only 3.88%, which influences little the heave motion. On the other hand, compared to the no-gap case in the main resonant region, the relative maximum values of the heave RAO occur near the main fluid resonant frequencies, which indicates that the fluid resonance plays a leading role in influencing the hydrodynamic characteristics of the moonpool in the main resonant region.

3.1.3 Wave forces on the moonpool

Figures 9(a), 9(c) show the horizontal and vertical wave forces on Body-A of different gap widths, respectively, whereas Figs. 9(b), 9(d) are for Body-B. The wave forces are nondimensionalized as follows:

$$F_x^A = \frac{F_{Ax}}{\rho g h H_0},\quad F_y^A = \frac{F_{Ay}}{\rho g h H_0},\quad F_x^B = \frac{F_{Bx}}{\rho g h H_0},$$

$$F_y^B = \frac{F_{By}}{\rho g h H_0} \tag{19}$$

where ρ is the fluid density, g is the gravity acceleration, h is the water depth and H_0 is the incident-wave height.

Again, the wave forces on the fixed moonpool are also shown in Figure 9 for comparison. Generally, for the heaving-free moonpool, the wave forces in the main resonant region are more sensitive to the change of the gap width, whereas they are insensitive to the change of the gap width in the secondary resonant region. As Fig. 9(a) illustrates, there is a wide range of the incident wave frequencies (when kh changes from 1.70 to 0.50), in which the Body-A is constantly acted by a relatively large horizontal wave force under the heaving-free conditions. Although the maximum vertical wave force on the fixed Body-A is larger than that under the heaving condition, this force quickly reduces to a negligible level (when kh changes from

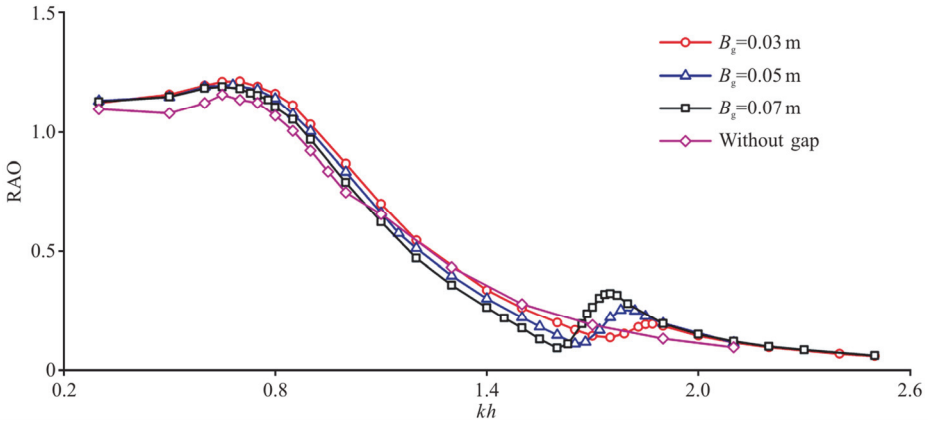

Fig. 8 (Color online) Heave RAO of the moonpool (d = 0.252 m , h = 0.5 m , H_0 = 0.024 m)

Table 7 Maximum of RAO in different gap widths

		B_g = 0.03 m	B_g = 0.05 m	B_g = 0.07 m	Without gap
The secondary resonant region	kh	0.70	0.68	0.65	0.65
	RAO	1.216	1.204	1.194	1.160
The main resonant region	kh	1.87	1.78	1.75	-
	RAO	0.195	0.255	0.323	-

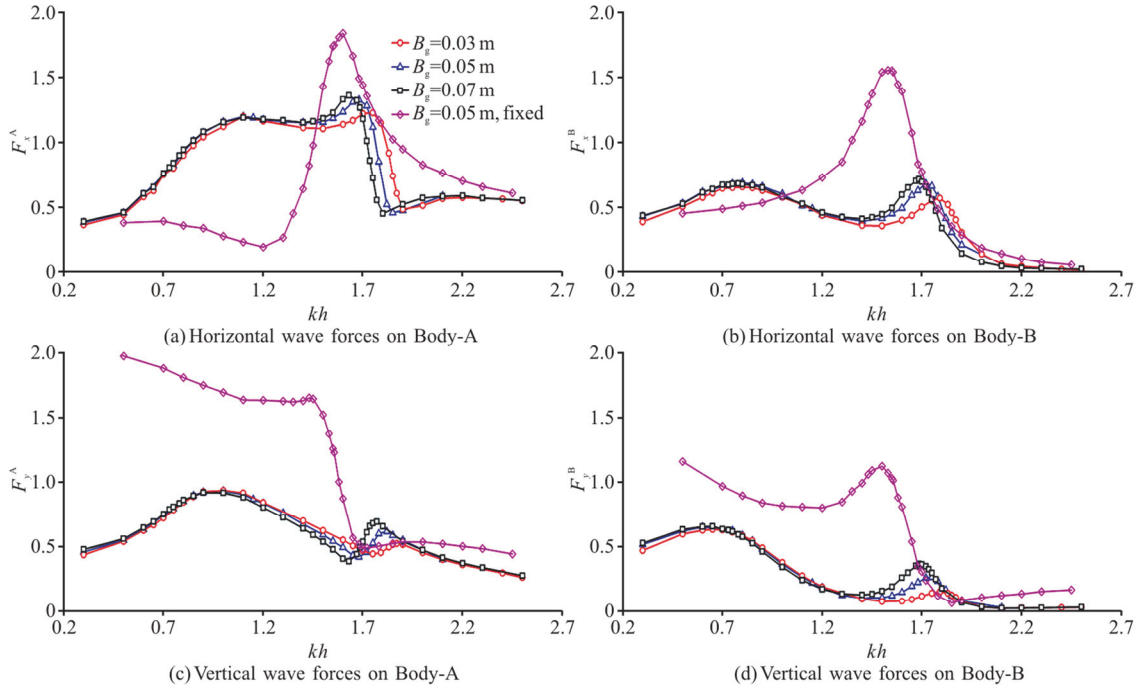

Fig. 9 (Color online) Comparison of wave forces on the moonpool at different widths of narrow gaps ($d = 0.252$ m , $h = 0.5$ m , $H_0 = 0.024$ m)

1.45 to 1.20). In brief, once the heaving-free side-by-side structures are acted by the incident waves in the secondary resonant region, the horizontal wave force on the upstream side of the body could be a threat to its structure life. Detailed discussion is presented in the next section.

As shown in Figure 9(b), the curves of the horizontal wave forces on the heaving Body-B have the same trend as the curves of the gap elevation in Fig. 7, and the maximum values of these horizontal wave forces all occur at the corresponding resonant frequencies, respectively. The gap elevation is still the

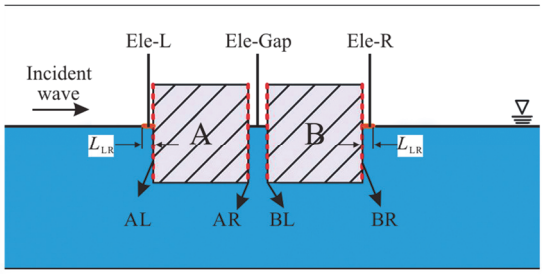

Fig. 10 (Color online) Arrangement of computational settings (Ele-L at upstream side, Ele-R at downstream side)

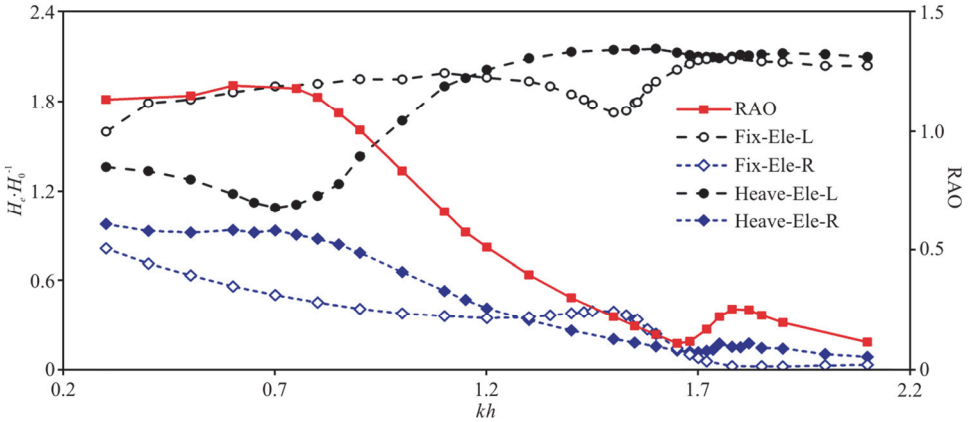

Fig. 11 (Color online) Comparison of the behaviors at Ele-L, Ele-R between the fixed and heaving-free moonpools (H_e is the wave elevation at each monitor, RAO is the response amplitude operator of the heaving-free moonpool, the left axis is for the wave elevation, the right axis is for the heave RAO)

main factor affecting the horizontal wave forces on the heaving Body-B in the secondary resonant region, similar to the case in the main resonant region[5].

From Fig. 9(c), it is noticed that in the secondary resonant region, another peak can be observed for the vertical wave forces on the heaving Body-A, with the maximum value near 0.556 at $kh = 1.00$. As for the fixed Body-A, its vertical wave force is a great deal larger than that of the heaving Body-A in the secondary resonant region, and will not tend to decrease with the decrease of kh in the studied range. Figure 9(d) presents a very similar pattern as that in Fig. 9(c). Detailed analysis of the fixed moonpool can be found in the previous work[17].

3.2 *Detailed comparison between fixed and heaving-free moonpools*

In Section 3.1, the secondary resonant region of the heaving-free moonpool is discussed. In this section a typical moonpool with $B_g = 0.05$ m, $d = 0.252$ m is considered. Detailed discussion will focuse on the comparison of the fixed and heaving-free moonpools.

3.2.1 The leading role of heave response in the secondary resonant region

Two new wave elevation monitors are added into the calculation as shown in Fig. 10, namely Ele-L, Ele-R, respectively. Ele-L, Ele-R are located at the upstream and downstream sides of the moonpool. To prevent the numerical oscillation, the areas of the length $L_{\mathrm{LR}} = 0.5B_g$ are considered in front of and behind the moonpool, and the average value of the free-surface elevation of all grids in each area is taken as the value of Ele-L, Ele-R, respectively. These two areas have been marked in orange color in Fig. 10.

Figure 11 presents the wave elevations of Ele-L, Ele-R for both the fixed and heaving-free moonpools. First, we consider the fixed moonpool. At most frequencies, the wave elevation of Ele-L is 1.8 times greater than the incident-wave height. Before the resonance frequency, the wave elevation on the downstream side decreases gradually with the increase of kh, because of the decreased wave transmission. Near the resonant frequency, the wave elevation on the upstream side and the downstream side reaches the minimum value and the maximum value, respectively. The two variation curves are very similar to those of the reflection coefficient and the transmission coefficient, because near the resonant point, more wave energy is used to excite the water resonance in the gap[11].

Secondly, we consider the heaving-free moonpool. Both Ele-L, Ele-R are greatly influenced by the heave response, especially in the secondary resonant

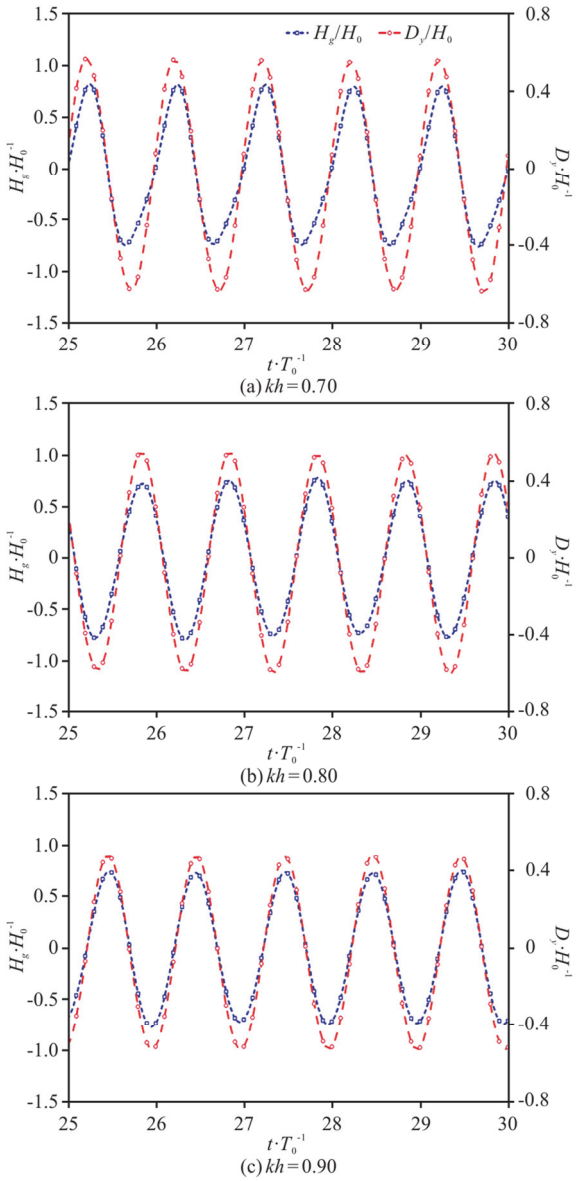

Fig. 12 (Color online) Wave elevation in the gap, heave motion (D_y) of three typical cases in the secondary resonant region (the left axis is for the gap wave elevation, the right axis is for the heave motion)

region. For comparison, the heave RAOs are also shown in Fig. 11. It can be seen that the heaving magnitude of the moonpool in the secondary resonant region is much larger than that in the main resonant region. The curves of Ele-L, Ele-R get closer to each other when the incident-wave frequency is near the secondary resonant point due to the heave motion of the moonpool, which indicates that the heave response dominates in influencing the fluid field. It must be emphasized that the wave elevations at the positions of the upstream monitor Ele-L and the downstream monitor Ele-R reach the minimum value and the maximum value, respectively, at both the main and

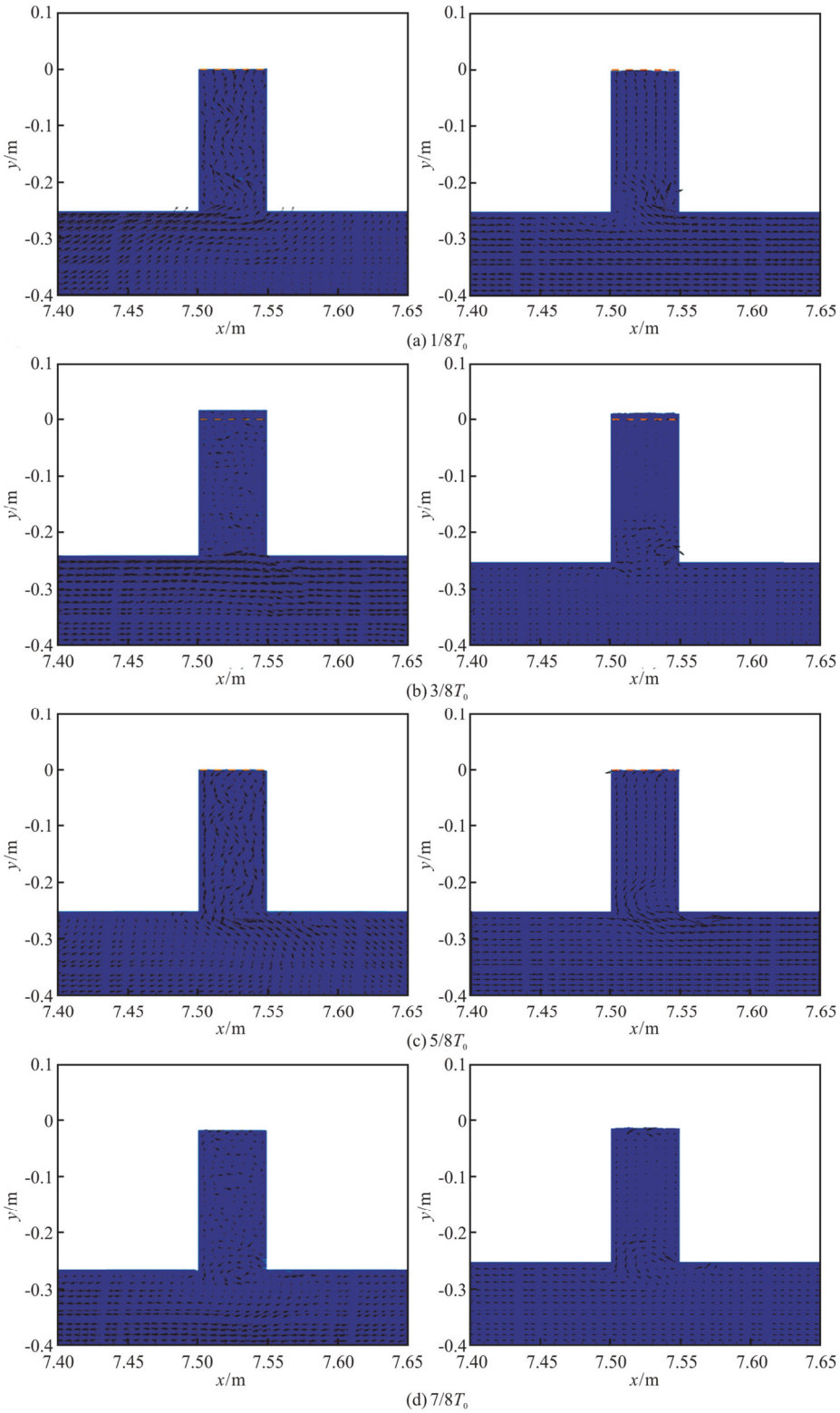

Fig. 13 (Color online) Velocity vectors around the narrow gap during a wave period (left side is for the heaving-free moonpool, right side is for the fixed moonpool, $B_g = 0.05$ m , $d = 0.252$ m , $kh = 0.80$)

secondary resonant points. The same pattern is observed as that for the fixed moonpool, which is easy to understand from the viewpoint of the conservation of energy. It is noted again that the gap resonance phenomenon of the heaving-free moonpool is the coupling of the incident-wave-induced excitation and the heave

response. It is reasonable to conclude that the heave response plays a leading role in exciting the secondary gap resonance.

To further confirm the above points, a detailed discussion is made for several typical cases of $kh =$ 0.70, 0.80 and 0.90. Figure 12 presents the heave motion and the gap elevation of three typical cases in the secondary resonant region, i.e., $kh = 0.80$ is the resonant point, $kh = 0.70$, 0.90 are the other two typical cases near the resonant point. It is easy to see that the heave motion and the gap elevation have the same phase in all three cases. Figure 13 presents the velocity vectors around the narrow gap ($B_g = 0.05$ m, $d = 0.252$ m) during a wave period at $kh = 0.80$, the left subfigures are for the heaving moonpool, the right side is for the fixed moonpool, in which, the dashed line represents the initial free surface. Figures 13(b), 13(d) show the two typical moments when the gap elevation reaches the peak and through, respectively. It is indicated by the heaving-free fluid field that the flow near the heaving moonpool is mainly affected by the large-magnitude-heaving motion. The vectors in the fluid field below the moonpool have vertical components with the same direction as that of the heave motion of the moonpool, whereas generally no vertical components are observed for the fixed moonpool. The coupling between the incident-wave exciting and the heave response affects the resonance of the moonpool. In the main resonant region, the incident-wave exciting dominates, whereas the heave response dominates in the secondary region.

3.2.2 Horizontal wave forces on each side of Body-A

With the notations in Fig. 10, the upstream side and the downstream side of Body-A, Body-B are marked as AL, AR and BL, BR, respectively. The horizontal wave forces on each side of Body-A, Body-B are separated to see why the horizontal wave forces (F_x^{A}, F_x^{B}) on the heaving-free moonpool are much different from those on the fixed one, especially, the remarkable large magnitude of F_x^{A} on the heaving-free moonpool at a low frequency.

Figures 14, 15 present the horizontal wave forces on the faces AL (F_x^{AL}), AR (F_x^{AR}) of Body-A for

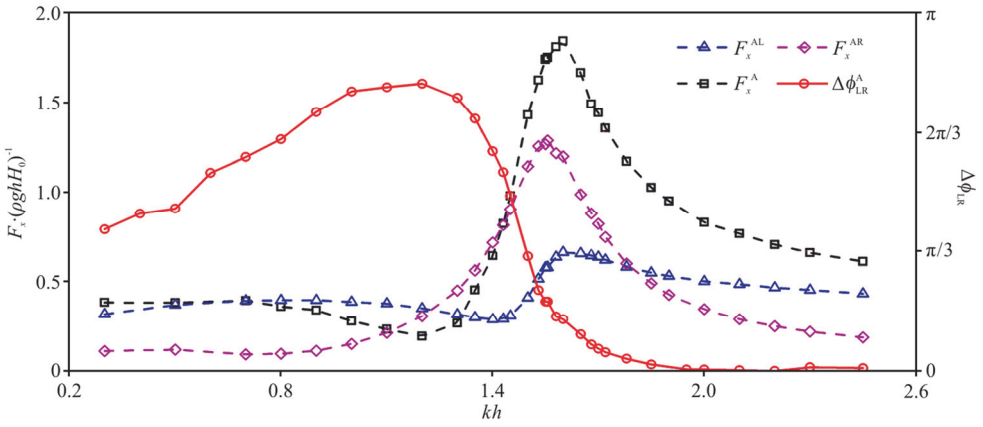

Fig. 14 (Color online) Horizontal wave forces and phase difference on the fixed Body-A (the left axis is for the horizontal wave forces, the right axis is for the phase difference)

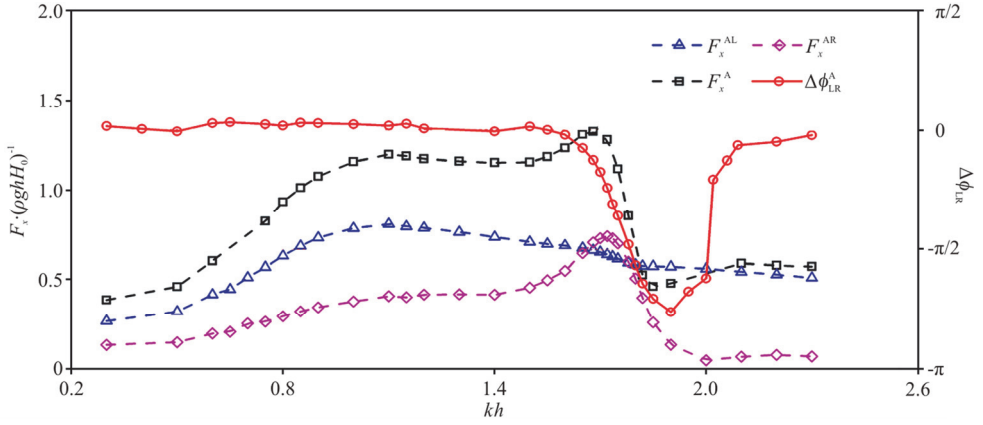

Fig. 15 (Color online) Horizontal wave forces on the heaving-free Body-A (the left axis is for the horizontal wave forces, the right axis is for the phase difference)

the fixed and heaving-free moonpools, respectively. It is shown that the horizontal wave forces are not always larger than F_x^{AL}, F_x^{AR} for both the fixed and heaving-free moonpools. It is easy to understand that F_x^{A} is decided by the coupling of both the magnitude and phase superpositions of F_x^{AL}, F_x^{AR}. Therefore,

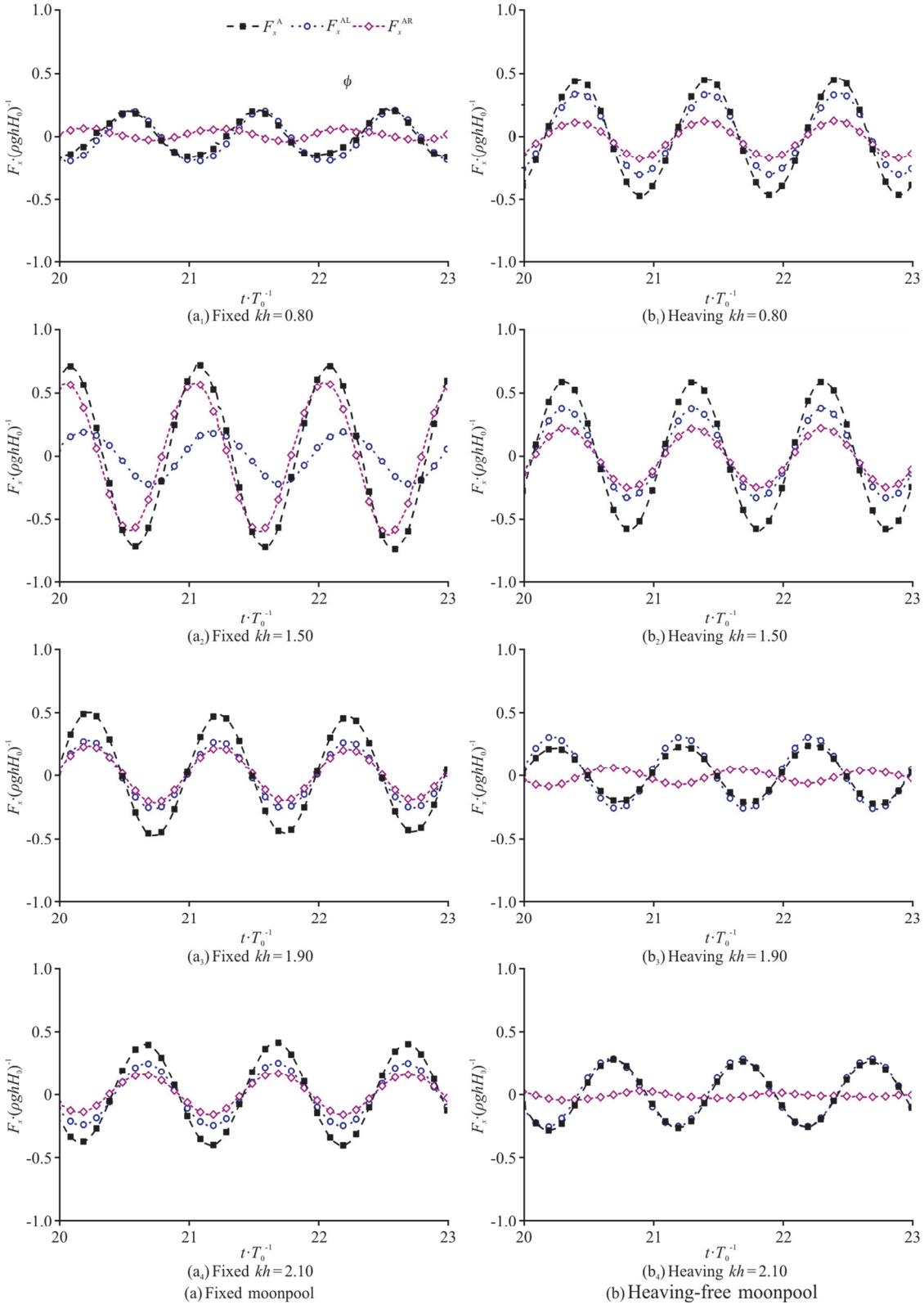

Fig. 16 (Color online) Time history of horizontal wave forces

the phase difference between F_x^{AL}, F_x^{AR} is also shown. The phase of F_x^{AL} is chosen as the reference, the phase difference is defined as

$$\Delta\phi_{LR} = \phi_L - \phi_R \tag{20}$$

where ϕ_L, ϕ_R are the phases of F_x^{AL}, F_x^{AR}, respectively, $\Delta\phi_{LR}$ is the phase difference between F_x^{AL}, F_x^{AR}, which is shown in Fig. 15.

The phase difference between F_x^{AL}, F_x^{AR} is also shown in Figs. 14, 15 as with the right axis for comparison. It can be seen from Fig. 14 that both F_x^{AL}, F_x^{AR} have a smaller magnitude than those on the heaving-free moonpool in the secondary resonant region, meanwhile, they also have a large phase difference. F_x^{A} is shown to have a remarkable low value. This phase difference decreases with the increase of kh, F_x^{A} reaches its maximum value at $kh = 1.6$, then, the phase difference quickly approaches near 0. F_x^{AL}, F_x^{AR} almost keep the same phase after $kh = 1.7$, which means F_x^{A} is only affected by the magnitudes of F_x^{AL}, F_x^{AR}. Therefore, in this range, F_x^{A} decreases slowly with kh.

As shown in Fig. 15, F_x^{AL}, F_x^{AR} almost keep the same phase before the main resonant frequency, because the heave response plays a leading role in affecting the fluid field in this range. Therefore, it is easy to understand the remarkable high magnitude of F_x^{A} in this region. When the incident frequency is higher than the main resonant frequency, the phase difference will increase with kh, and reaches the maximum value at $kh = 1.90$. Also, this phase difference quickly reduces to approach near 0 after $kh = 2.10$. The existence of the phase difference leads to the rapid decrease of F_x^{A} after $kh = 1.68$. To show the coupling of the magnitude and phase differences between F_x^{AL}, F_x^{AR} more directly, the time histories of F_x^{A}, F_x^{AL} and F_x^{AR} are presented in Fig. 16 for both the fixed and heaving-free moonpools at the typical incident-wave frequencies of $kh = 0.80$, 1.50, 1.90 and 2.10.

3.2.3 Horizontal wave forces on each side of Body-B

It is seen from Fig. 9(b) that the difference of the horizontal wave force on Body-B (F_x^{B}) between the fixed and the heaving-free moonpools is not such conspicuous as that of F_x^{A}. Figures 17, 18 show the horizontal wave forces on the faces BL, BR (F_x^{BL}, F_x^{BR}) and their phase difference for the fixed and heaving-free moonpools, respectively. As shown in Fig. 17, F_x^{B}, F_x^{BL} and F_x^{BR} have the same trend in the studied range, they all reach the maximum value at the resonant point, which can be explained by the phase difference. In the range from $kh =$ 0.6 to 2.0, the phase difference keeps at a relatively stable and small level. Although the phase difference is much changed out of this range, the magnitudes of F_x^{BL}, F_x^{BR} approach a very low level.

Figure 18 shows F_x^{BL}, F_x^{AR} and their phase difference for the heaving-free moonpool. Similar to the fixed cases, a large phase difference happens with the very small F_x^{AR}. Therefore, F_x^{B}, F_x^{BL} are almost the same after the main resonant frequency. Before the main resonant frequency, the phase difference keeps near 0, due to the heave response as explained in detail before. The phase difference affects little F_x^{B}. Detailed time histories of F_x^{B}, F_x^{BL} and F_x^{BR} are shown here.

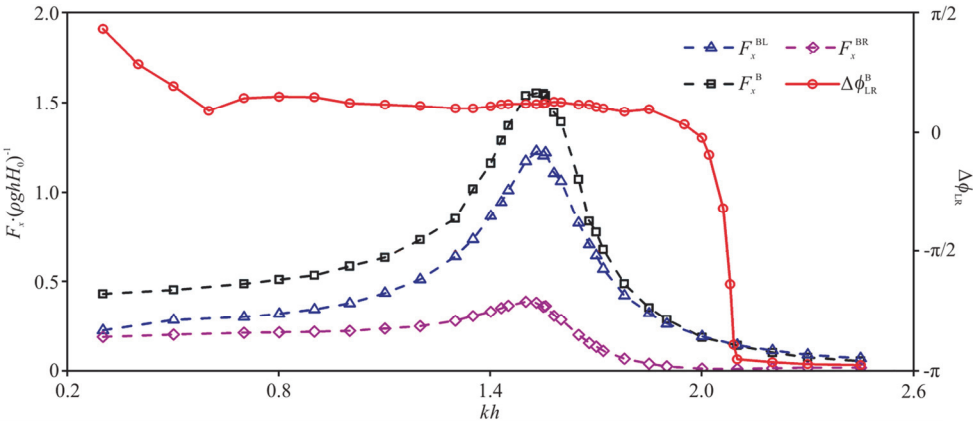

Fig. 17 (Color online) Horizontal wave forces and phase difference on the fixed Body-B (the left axis is for the horizontal wave forces, the right axis is for the phase difference)

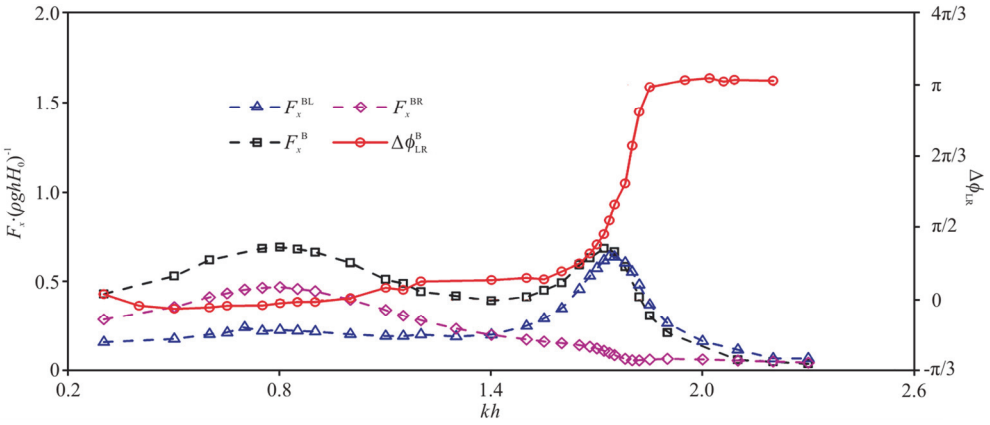

Fig. 18 (Color online) Horizontal wave forces and phase difference on the heaving-free Body-B (the left axis is for the horizontal wave forces, the right axis is for the phase difference)

3.3 *Hydrodynamic resonance for the heaving-free moonpool with different body drafts*

We have already made the parameter study of the gap width with the corresponding discussions of the secondary resonant region. The body draft is another important factor to influence the gap resonance phenomenon[5], therefore, we make the parameter study of the body draft with consideration of the secondary resonant region in this section.

3.3.1 Gap resonance and heave response of the moonpool

To investigate the effects of the body draft on the fluid resonance, we consider the heaving-free moonpool with a constant gap width, $B_g = 0.05$ m, for three different body drafts ($d = 0.103$ m, 0.153 m and 0.252 m). Figure 19 shows the computed gap elevations for the narrow gap with different drafts, and Table 8 lists the resonant frequencies in different cases and the corresponding gap elevations. It is shown that the gap elevation is more sensitive to the draft in the main resonant region than in the secondary resonant region. However, the draft change plays a much more important role in the secondary resonant region than the factor of the gap width. In the secondary resonant region, the resonant frequency decreases with the increase of the body draft because of the increase of the volume of water in the gap, which is similar to the case in the main resonant region[5]. At the same time, the resonant magnitude

Table 8 Resonant frequency and amplitude for different body drafts

		$d = 0.103$ m	$d = 0.153$ m	$d = 0.252$ m
The secondary resonant region	kh	1.00	0.90	0.80
	H_g / H_0	1.145	1.267	1.537
The main resonant region	kh	3.30	2.50	1.75
	H_g / H_0	1.703	1.877	2.445

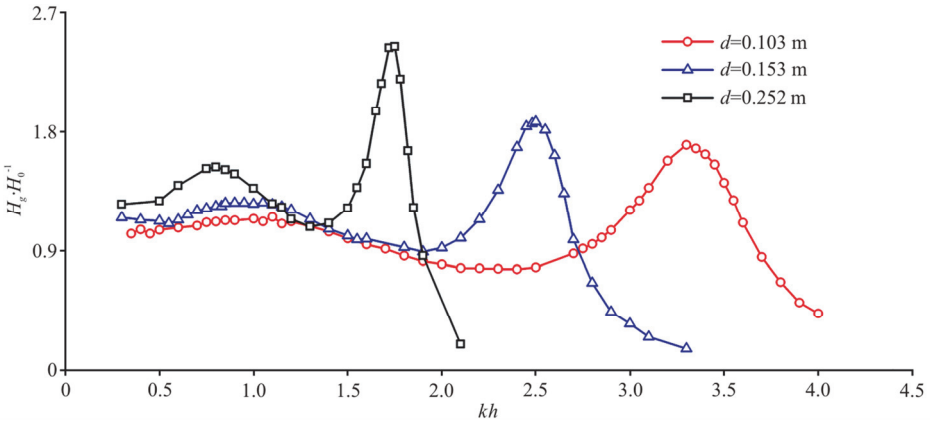

Fig. 19 (Color online) Wave elevation in the narrow gap with different body drafts ($B_g = 0.05$ m , $h = 0.5$ m , $H_0 = 0.024$ m)

increases with the body draft. Similar to the case in the secondary resonant region discussed in Section 3.2.1, the heave motion has a large amplitude and plays a leading role in influencing the gap field.

The heave RAOs of the heaving-free moonpool are shown in Fig. 20. Similar to the results of the gap elevation, the resonant frequencies of the moonpool with different drafts show a large shift in the main resonant region. However, in the range of $0.20 < kh < 1.00$, i.e., in the secondary resonant region, the heave RAO gradually increases with the body draft, which actually reflects the magnitude of the vertical wave force on the whole moonpool.

3.3.2 Wave forces on the moonpool

The wave forces acting on the heaving-free moonpool with three different body drafts are shown in Fig. 21. From Figs. 21(a), 21(b), it is shown that the horizontal wave forces on each body increase with the increase of the draft due to the increment of the wet area in general. When the body draft increases, the horizontal wave forces change more rapidly with the incident wave frequency. Again, the horizontal wave forces show a similar trend as the gap elevation curves in the cases of all three drafts.

For the vertical wave forces, it can be seen in Figs. 21(c), 21(d) that the vertical wave forces in the secondary resonant region are much larger than those in the main resonant region. The ratios of the maximum vertical wave forces on Body-A in the secondary resonant region to those in the main resonant region are 1.75, 1.76 and 1.51 for $d = 0.103$ m, 0.153 m and

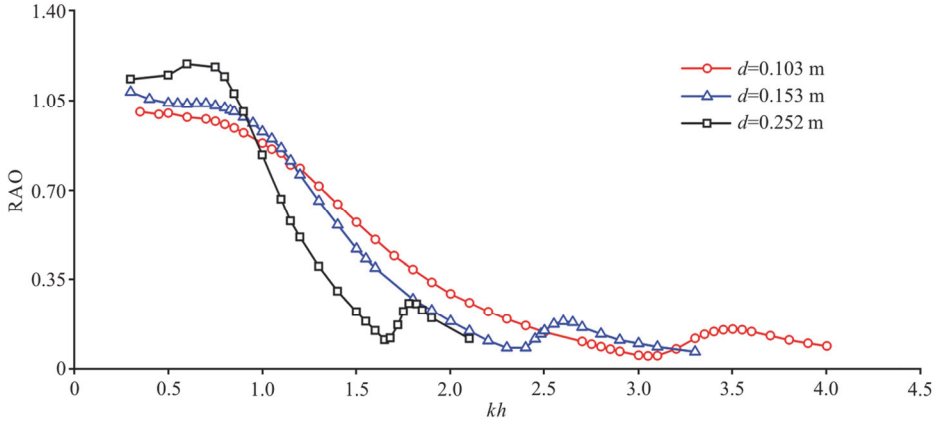

Fig. 20 (Color online) Heave RAOs of the moonpool with different body drafts ($B_g = 0.05$ m, $h = 0.5$ m, $H_0 = 0.024$ m)

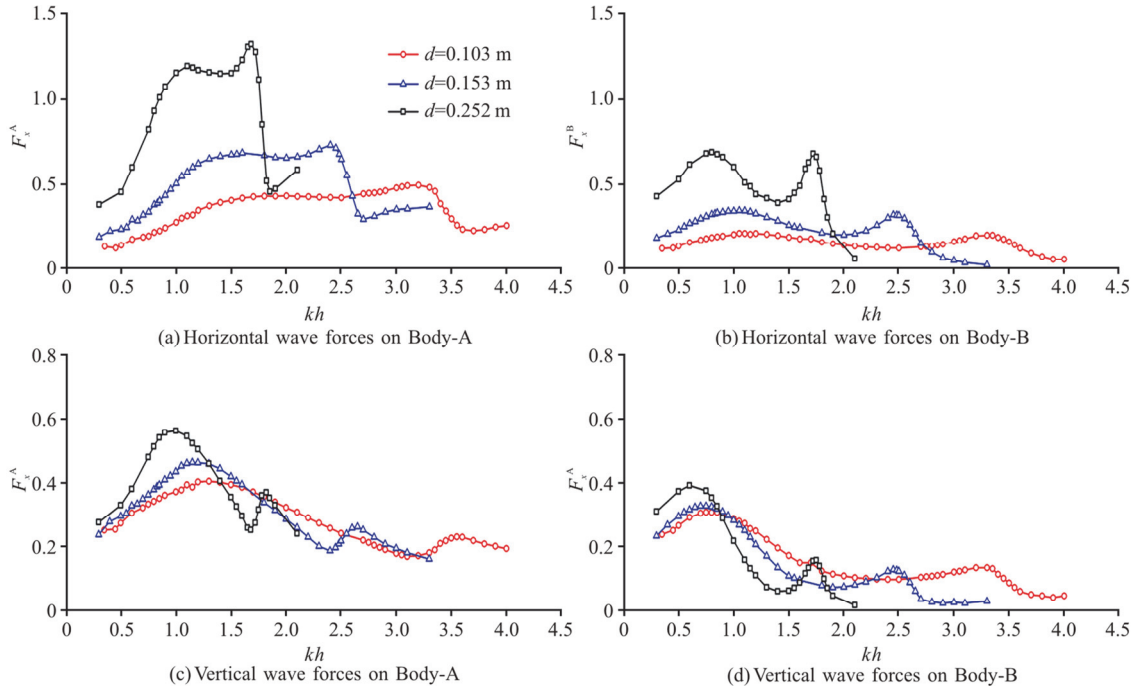

Fig. 21 (Color online) Wave forces on the moonpool with different body drafts ($B_g = 0.05$ m , $h = 0.5$ m , $H_0 = 0.024$ m)

0.252 m, respectively, while the ratios for Body-B are 2.28, 2.54 and 2.47 for $d = 0.103$ m, 0.153 m and 0.252 m, respectively.

4. Conclusions

In this paper, a CIP-based numerical model is established for the piston-mode fluid resonance of a heaving-free moonpool in the beam sea. The numerical model is first validated by the correlation factor method. A new resonant region of the heaving-free moonpool is identified, namely the secondary resonant region. Corresponding characteristics of the secondary resonant region are discussed. Meanwhile, the parameter studies of the gap width and the body draft are conducted, and the following conclusions can be drawn:

(1) The developed CIP-based numerical model enjoys a low level of uncertainty referring to both the time step and the grid size. The free-surface elevation in the gap is sensitive to both the time-step resolution and the grid size resolution, and the heave motion is more sensitive to the grid size resolution.

(2) Two resonant regions for the heaving-free moonpool are identified. The main resonant region is mainly induced by the excitation of the incident waves located near the resonant region of the fixed moonpool. The secondary resonant region is mainly induced by the heave motion, at a lower frequency than that of the main resonant region.

(3) The extremum value of the free-surface elevation at the upstream and the downstream of the moonpool is always obtained near the resonant frequencies, for both the main and secondary resonant regions.

(4) Significant differences of the hydrodynamic characteristics between the heaving-free and fixed moonpools are observed in both the main and secondary resonant regions. Especially, the heaving-free Body-A is acted by a large horizontal wave force in a wide range of incident-wave frequencies, due to the influence of the phase difference between F_x^{AL}, F_x^{AR}, which may be a challenge in engineering applications. At the same time, the phase difference has little impact on F_x^{B}.

The present paper focuses on the hydrodynamic resonance of a heaving-free moonpool with a narrow gap, which is very close to the situation in the actual application. The suggested secondary resonant region provides a new way to reduce the negative effects of the gap resonance in the lower frequency beam sea. The characteristics of the heaving-free moonpool are shown through the influence of the heave motion on the fluid field and the influence of the phase difference on the horizontal wave forces. While the secondary resonant region is mainly induced by the heave response, further research on other kinds of movements in the moonpool at the low wave frequency is desirable in future.

Acknowledgements

This work was supported by the Fundamental Research Funds for the Central Universities (Grant No. HIT.OCEF.2021037), the Taishan Scholars Project of Shandong Province (Grant No. tsqn201909172) and the University Young Innovational Team Program, Shandong Province (Grant No. 2019KJN003).

References

[1] Liang H., Chua K. H., Wang H. et al. Numerical and experimental investigations into fluid resonance in a gap between two side-by-side vessels [J]. *Applied Ocean Research*, 2021, 111: 102581.

[2] Ning D. Z., Su X. J., Zhao M. et al. Numerical study of resonance induced by wave action on multiple rectangular boxes with narrow gaps [J]. *Acta Oceanologica Sinica*, 2015, 34(5): 92-102.

[3] He G., Teng B., Li B. et al. Research on the hydrodynamic influence from the gaps between three identical boxes by a scaled boundary finite element method [J]. *Journal of Hydrodynamics*, 2006, 21(3): 418-424.

[4] Feng X., Chen X., Dias F. A potential flow model with viscous dissipation based on a modified boundary element method [J]. *Engineering Analysis with Boundary Elements*, 2018, 97: 1-15.

[5] He G., Jing P., Jin R. et al. Two-dimensional numerical study on fluid resonance in the narrow gap between two rigid-connected heave boxes in waves [J]. *Applied Ocean Research*, 2021, 110(2): 102628.

[6] Fredriksen A., Kristianse T., Faltinsen O. Wave-induced response of a floating two-dimensional body with a moonpool [J]. *Philosophical Transactions of the Royal Society of London A Mathematical Physical and Engineering Sciences*, 2015, 373(2033): 201401097.

[7] Tan L., Lu L., Tang G. Q. et al. A dynamic solution for predicting resonant frequency of piston mode fluid oscillation in moonpools/narrow gaps [J]. *Journal of Hydrodynamics*, 2020, 32(1): 54-69.

[8] Tan L., Lu L., Tang G. Q. et al. A viscous damping model for piston mode resonance [J]. *Journal of Fluid Mechanics*, 2019, 871: 510-533.

[9] Lu L., Teng B., Cheng L. et al. Modelling of multi-bodies in close proximity under water waves-Fluid resonance in narrow gaps [J]. *Ocean Engineering*, 2011, 38(13): 1403-1416.

[10] Ning D., Yi Z., Zhang C. et al. Experimental and numerical study on wave response at the gap between two barges of different draughts [J]. *Applied Ocean Research*, 2018, 77: 14-25.

[11] Gao J., Zang J., Chen L. et al. On hydrodynamic characteristics of gap resonance between two fixed bodies in close proximity [J]. *Ocean Engineering*, 2019, 173: 28-44.

[12] Jiang S. C., Gu Q., Cong P. W. Fluid resonance in the narrow gap of a box-wall system under cnoidal wave action [J]. *Ocean Engineering*, 2021, 238: 109774.

[13] Takewaki H., Nishiguti A., Yabe T. Cubic interpolated pseudo-particle method (CIP) for solving hyperbolic-type equations [J]. *Journal of Computational Physics*, 1985, 61(2): 261-268.
[14] Hu C., Kashiwagi M. A CIP-based method for numerical simulations of violent free-surface flows [J]. *Journal of Marine Science and Technology*, 2004, 9(4): 143-157.
[15] Zhao X., Chen Y., Huang Z. et al. A numerical study of tsunami wave impact and run-up on coastal cliffs using a CIP-based model [J]. *Natural Hazards and Earth System Sciences*, 2017, 17(5): 641-655.
[16] He G. A new adaptive Cartesian-grid CIP method for computation of violent free-surface flows [J]. *Applied Ocean Research*, 2013, 43: 234-243.
[17] He G., Zhang J., Zhang D. Hydrodynamic resonance from narrow gap between twin floating bodies by CIP viscous model [J]. *Journal of Harbin Engineering University*, 2019, 40(1): 58-64(in Chinese).
[18] Faltinsen O., Rognebakke O., Timokha A. Two-dimensional resonant piston-like sloshing in a moonpool [J]. *Journal of Fluid Mechanics*, 2007, 575: 359-397.
[19] Fredriksen A. G., Kristiansen T., Faltinsen O. M. Experimental and numerical investigation of wave resonance in moonpools at low forward speed [J]. *Applied Ocean Research*, 2014, 47: 28-46.
[20] Li Y., Zhang C. Analysis of wave resonance in gap between two heaving barges [J]. *Ocean Engineering*, 2016, 117: 210-220.
[21] Perić M., Swan C. An experimental study of the wave excitation in the gap between two closely spaced bodies, with implications for LNG offloading [J]. *Applied Ocean Research*, 2015, 51: 320-330.
[22] Zhang C., Sun X., Ding Z. et al. Hydrodynamics of a floating barge adjacent to fixed structure in transient wave fronts [J]. *Physics of Fluids*, 2021, 33(10): 107106.
[23] Guo X., Lu H., Yang J. et al. Resonant water motions within a recessing type moonpool in a drilling vessel [J]. *Ocean Engineering*, 2017, 129: 228-239.
[24] Molin B. On the piston and sloshing modes in moonpools [J]. *Journal of Fluid Mechanics*, 2001, 43: 27-50.
[25] Hu C., Kashiwagi M. Two-dimensional numerical simulation and experiment on strongly nonlinear wave-body interactions [J]. *Journal of Marine Science and Technplogy*, 2009, 14(2): 200-213.
[26] Ha T., Lin P., Cho Y. Generation of 3D regular and irregular waves using Navier–Stokes equations model with an internal wave maker [J]. *Coastal Engineering*, 2013, 76: 55-67.
[27] Xiao F., Honma Y., Kono T. A simple algebraic interface capturing scheme using hyperbolic tangent function [J]. *International Journal for Numerical Methods in Fluids*, 2005, 48(9): 1023-1040.
[28] Chen L., He G., Zhang J. et al. Analysis on the hydrodynamic resonance of fixed rectangular boxes with narrow gaps by a constrained interpolation profile method [C]. *Proceedings of the 28th International Ocean and Polar Engineering Conference*, Sapporo, Japan. 2018, 358-364.
[29] Chen L., He G., Bingham H. et al. Gap resonance of fixed floating multi caissons [C]. *Proceedings of the 38th International Conference on Ocean, Offshore and Arctic Engineering*, Glasgow, UK. 2019.
[30] Wang J., Liu P., Chin C. et al. Parametric study on hydroelasticity characteristics of auto-pitch wing-in-ground effect oscillating foil propulsors [J]. *Ocean Engineering*, 2020, 201: 107115.
[31] Saitoh T., Miao G., Ishida H. Theoretical analysis on appearance condition of fluid resonance in a narrow gap between two modules of very large floating structure [C]. *Proceedings of the Third Asia-Pacific Workshop on Marine Hydrodynamics*, Shanghai, China, 2006, 170-175.